THE M_W 6.7 GEORGE SOUND EARTHQUAKE OF OCTOBER 15, 2007: RESPONSE AND PRELIMINARY RESULTS

Tanja Petersen[1], John Ristau[1], John Beavan[1], Paul Denys[2], Mike Denham[2], Bryan Field[1], Caroline François-Holden[1], Rob McCaffrey[3], Neville Palmer[1], Martin Reyners[1], Sergey Samsonov[4], and The GeoNet team[1]

ABSTRACT

The M_w 6.7 George Sound earthquake of October 15, 2007, occurred only a few kilometres offshore of Fiordland, within a region where the subduction zone of the Australian Plate beneath the Pacific Plate intersects the offshore extension of the Alpine Fault. Rapid response deployments of portable seismographs, a strong motion recorder and GPS receivers relatively close to the epicentre soon after the main shock allowed us to relate the event to thrusting at the subduction interface. The main shock moment tensor solution places the event at a shallow depth of 21 km. The sequence of aftershocks that followed the main event presents predominantly reverse faulting mechanisms with depths of 20 to 25 km. Earthquake re-locations using data recorded by the portable seismometers reveal a cluster of aftershocks at 17 to 25 km. This cluster defines a steeply SE-dipping plane, while another cluster at about 7-12 km depth images a NW-dipping plane within the overlying plate. Preliminary results from the seismic, geodetic and near-field strong motion geophysical data are consistent with rupture on an east dipping fault plane, presumed to be the subduction interface.

INTRODUCTION

On 15 October 2007 at 12:29 UT (12:29am on October 16 local time) a shallow M_w 6.7 earthquake shook the Fiordland region of New Zealand. The earthquake epicentre was located about 12 km offshore in the vicinity of George Sound, approximately 50 km southwest of Milford Sound, at a preliminary depth of 24 km. An aftershock sequence that included one M_w 6.0 (M_L 6.2) earthquake followed the main shock and lasted for several weeks. The New Zealand GeoNet network of seismographs recorded the main shock across the whole of New Zealand. Earthquake amplitudes from 107 stations were used to calculate the local magnitude and ground shaking intensities (Figure 1a); waveforms recorded by stations closest to the earthquake were clipped. A ground shaking of MM8 near the epicentre was estimated. This relatively large earthquake was reported to be felt widely in New Zealand (Figure 1b), but the damage to buildings and infrastructure was minor as the epicentre was offshore and the Fiordland region is largely unpopulated.

Earthquakes of this size have been experienced in Fiordland in the past. Over the last 20 years there have been five earthquakes of similar magnitude within the Fiordland region. These are the M_w 6.7 (depth 60 km) Te Anau earthquake of 1988, the M_W 6.4 (depth 24 km) Doubtful Sound earthquake of 1989, the M_W 6.8 (depth 22 km) Secretary Island earthquake of 1993, the M_W 6.1 (depth 18 km) Thompson Sound earthquake of 2000 and the M_W 7.2 (depth 18 km)

Secretary Island earthquake of 2003. The deeper 1988 Te Anau earthquake was related to internal stresses in the subducted plate [1]. The 2000 Thompson Sound earthquake was also an intraplate event that was due to deformation within the overlying plate [2], while the other shallower earthquakes within the sequence were directly associated with the plate convergence [3; 4].

The Fiordland region of New Zealand is located at a highly oblique convergent boundary between the Australian and the Pacific tectonic plates. [5] provide an excellent overview of the tectonics of Fiordland; however, some salient points follow. There are two features capable of generating large earthquakes in the area, the Puysegur subduction zone (dip-slip), located off the south coast of Fiordland, and the offshore extension of the Alpine Fault (strike-slip). The present-day relative motion of the Australian plate with respect to the Pacific plate is 39 mm per annum at 65° azimuth [6] and the long-term rate is 36 mm/yr at 66° azimuth (3 Myr-average NUVEL-1A rate [7]). [8] relocated earthquakes in the area, including deep events that extend to depths of 150 km, and found that the subduction zone steepens markedly north of Doubtful Sound becoming almost vertical below about 30 km south of Milford Sound. This steepening was shown to coincide with a change in the average strike of the subducted slab from 23° to 40° [9].
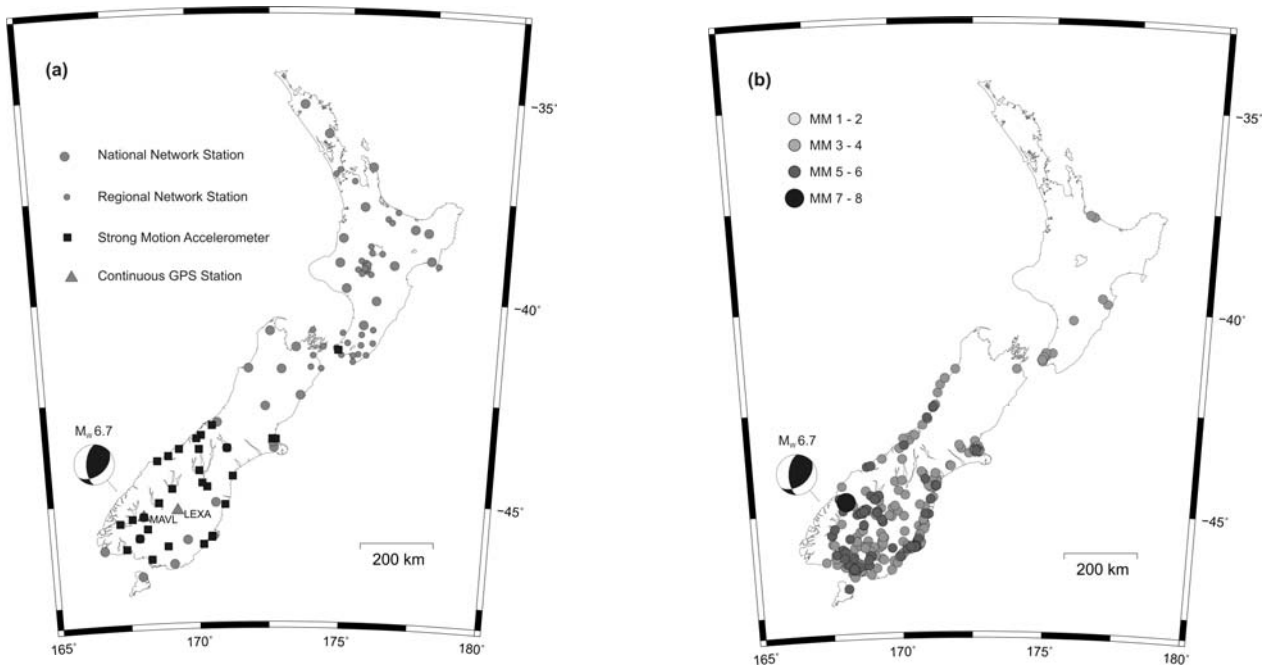
In order to better understand the nature and settings of the 2007 George Sound earthquake, GeoNet deployed five

[1] *GNS Science, Lower Hutt*

[2] *School of Surveying, Otago University, Dunedin*

[3] *now at Rensselaer Polytechnic Institute, New York*

[4] *also at University of Western Ontario, Canada*

Figure 1: *a) The 107 GeoNet network stations that triggered the GeoNet earthquake detection system by recording the 2007 George Sound main shock: 27 triggered strong motion accelerometers, 4 continuously recorded accelerometers, 36 short-period seismometers and 40 broadband seismometers. All clipped broadband instruments are excluded. The continuous GPS stations MAVL and LEXA recorded displacements above noise level. b) The GeoNet website [http://www.geonet.org.nz] received 1549 electronically-submitted felt reports for the main shock, ranging from MM3 up to one report of MM7. Note that there are no felt reports for the north-central South Island.*

portable short-period seismometers along the Fiordland coast, near the epicentre. In addition, campaign and continuous GPS and InSAR data were acquired. This report outlines our response to the 2007 George Sound earthquake, and presents preliminary results from analyses of the main shock and its aftershock sequence using seismic, geodetic and near-field strong motion data.

RAPID RESPONSE

The GeoNet project is a programme and group within GNS Science modernising New Zealand geological hazard monitoring systems (http://www.geonet.org.nz). The project started in 2001 and at present includes an earthquake monitoring network that consists of 46 broadband seismometers and 74 short-period seismometers recording continuous data in real-time. A network of 199 strong motion accelerographs provides triggered data. GeoNet also operates a network of about 120 continuously-recording GPS (cGPS) sites, 31 of these in partnership with Land Information New Zealand. Seven of the cGPS sites are located in the southern South Island below 44°S.

The 2007 George Sound main shock triggered 27 of the 199 strong motion accelerometers, mostly in the southern half of the South Island, and was recorded by seismometers distributed across the entire mainland of New Zealand (Figure 1a). Coseismic displacements were recorded well above the noise level at two cGPS sites, and were detectable at several other sites.

Following the main shock, a GeoNet team deployed five portable short-period seismometers and one triggered strong motion accelerometer in order to gain improved locations for the expected aftershock sequence. The instruments were more or less evenly distributed along the Fiordland coast between Caswell Sound and Milford Sound (Figure 2). The remoteness of the area together with poor weather conditions did not allow for an instrument deployment before 17 October 2007. The instruments were retrieved on 27 November 2007.

A GNS/Otago University team reoccupied a set of 19 survey-mode GPS sites in the vicinity of the earthquake from 11-15 November 2007, in order to measure the near-field coseismic displacements for subsequent use in defining the earthquake fault. These sites had most recently been surveyed in February 2006, with some observed as recently as December 2006. The 4-week delay after the earthquake means that the observations include the first four weeks of postseismic motion (if any) as well as the coseismic motion of the main shock and any large aftershocks. The observations also require a correction for the steady interseismic motion between surveys.

As well as these field responses, we collected and processed three pre-earthquake and two post-earthquake images from the Phased Array type L-band Synthetic Aperture Radar (PALSAR) instrument on the Advanced Land Observing Satellite (ALOS). Space-borne Differential Interferometric Synthetic Aperture Radar (DInSAR) is capable of measuring ground deformation over a large area (70-100 km² extent) with high spatial resolution (7-30 m) and high accuracy (0.5-2 cm) [e.g., 10; 11].
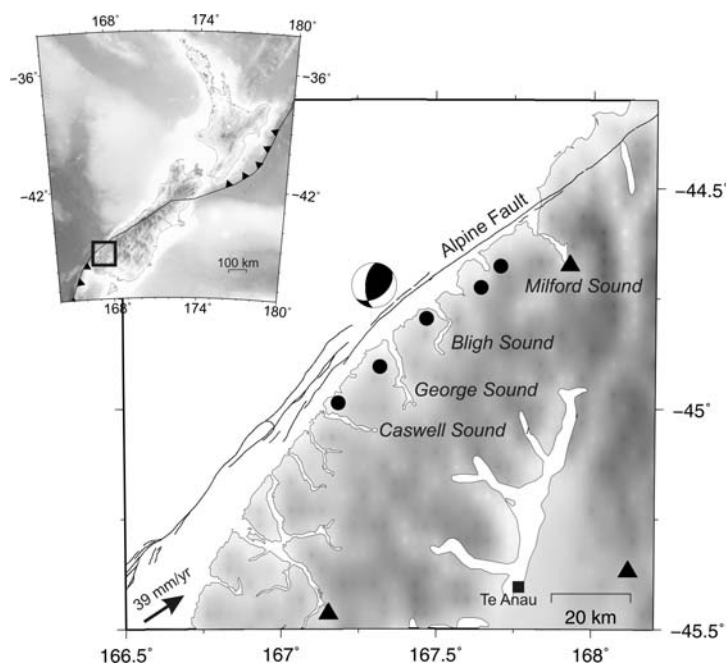
Figure 2: *Map of area around the M_W 6.7 George Sound earthquake located offshore of Fiordland, New Zealand. The portable short-period seismometers (circles) deployed as part of the GeoNet aftershock response and permanent GeoNet network stations (triangles) are marked in black. The earthquake occurred within an area where the Alpine Fault intersects the subduction of the Australian Plate beneath the Pacific Plate at a rate of about 39 mm/yr.*

FELT EFFECTS AND DAMAGE

GeoNet received 1,549 reports of people feeling the main shock. These people filled in an electronic form on the GeoNet website (http://www.geonet.org.nz), and from their answers Modified Mercalli (MM) intensities were calculated for the felt shaking. The spatial distribution of the shaking felt is shown in Figure 1b. With the exception of the one MM7 report, damage was minor, limited to objects falling off shelves. The MM7 report came from Hollyford, located about 20 km east of Milford Sound, describing some heavy radio equipment falling over. There were also five MM6 reports from Queenstown, Wanaka, Te Anau and Milford Sound. The earthquake was felt (MM4-5) as far south as Stewart Island and as far north as Tauranga (MM3-4). There were no felt reports from the populated north-central South Island, suggesting that seismic energy was de-focused by geological features of the Southern Alps. A similar observation was reported by [5].

MOMENT TENSOR SOLUTIONS

High quality seismic broadband data recorded by the GeoNet network was used to calculate centroid moment tensor (CMT) solutions for the 2007 George Sound main shock and some of the larger aftershocks. A brief description of the moment tensor method is given here; [12] provides a detailed overview of the regional moment tensor method in New Zealand. In 2003 the GeoNet project began a major upgrade to the New Zealand seismograph network, and currently there are more than 40 three-component broadband seismometers in New Zealand that provide high quality seismic data suitable for regional moment tensor analysis. It is now possible to routinely calculate moment tensor solutions for New Zealand earthquakes with $M_W \geq \sim 3.5 - 4.0$. Regional CMT solutions at GeoNet are calculated using code developed by Doug Dreger

at the University of California, Berkeley Seismological Laboratory [13; 14; 15]. Regional CMT analysis differs from teleseismic moment tensor analysis (e.g. Global CMT Project or USGS moment tensor solutions) in two important ways. First, only regional waveform data (source-receiver distances of 1000 km or less) are used, and second, region-specific velocity models are required. For M ≤ ~ 5.0, there is little very low-frequency energy in the waveforms and the velocity model used to calculate the Green's functions becomes more important. Because the inversion utilizes waveforms from all three components, it can be done using only a few stations, although a greater number of stations with a good azimuthal distribution is preferred to reduce the effects of 3D structure.

Fault mechanisms for earthquakes in the Fiordland region are quite varied, reflecting the complexity of the tectonics in the region (Figure 3). However, the largest shallow earthquakes have been primarily reverse faulting mechanisms. Ten CMT solutions were calculated for the 2007 George Sound sequence with M_w 3.9 – 6.7 (Figure 3; Table 1). The two largest events (M_w 6.7 and M_w 6.0) also had CMT solutions calculated by the Global CMT Project, which agree well with the GeoNet CMT solutions. The observed waveforms and the Green's functions for the main shock and the largest aftershock were bandpass filtered at 0.01 – 0.033 Hz, which provided a good signal-to-noise ratio. The remaining aftershocks were bandpass filtered at 0.03 – 0.06 Hz, 0.04 – 0.08 Hz, or 0.05 – 0.10 Hz depending on the signal-to-noise ratio. Figure 4 shows the location and focal mechanism of the main shock, and the stations used to calculate the CMT. Most of the broadband station records in the southern half of the South Island were clipped during the event and could not be used in the CMT solution. The observed and synthetic waveform fits were excellent for all of the stations used (Figure 4). For the main shock, solutions were calculated every kilometre over a depth range of 2 – 30 km to find the solution with the largest variance reduction between the observed and synthetic waveforms. The best fit is at 21 km depth with an estimated error of ~ ± 4 km (Figure 4). At depths greater than ~ 15 km
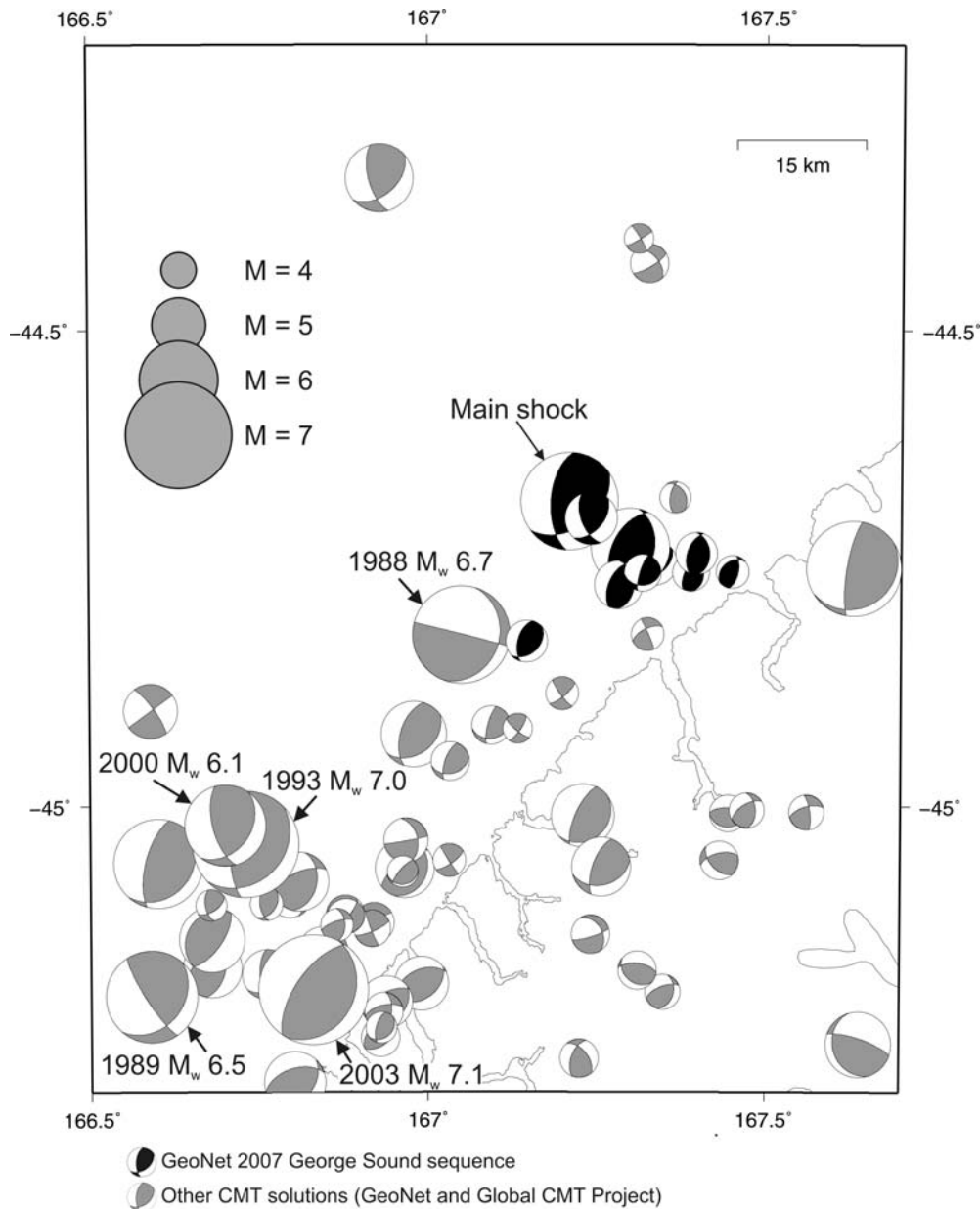
Figure 3: Focal mechanisms from CMT solutions for earthquakes in the Fiordland region. The George Sound sequence events (black) are all mainly reverse faulting mechanisms with depths of 20 – 25 km. Most of the large shallow earthquakes in the region are also reverse faulting events, while the smaller events have a variety of mechanisms and orientations.

Table 1.George Sound moment tensor solutions

| Date	Latitude	Longitude	S/D/R (NP1)	S/D/R (NP2)	ML	Mw	Mo	CD
200710151229	-44.7214	167.3019	190/52/64	48/45/119	6.7	6.7	1.33E+19	21
200710151734	-44.7446	167.3356	173/62/50	53/47/140	4.9	4.5	7.25E+15	18
200710151922	-44.8269	167.1464	196/56/71	48/39/116	4.9	4.4	4.77E+15	20
200710152128	-44.7285	167.2994	207/53/99	12/38/79	6.2	6.0	9.67E+17	20
200710152304	-44.7548	167.3888	206/64/108	348/31/57	4.5	4.1	1.40E+15	20
200710160026	-44.7346	167.3976	200/54/104	356/39/71	4.9	4.4	5.24E+15	20
200710161434	-44.7677	167.2820	204/57/103	1/35/71	5.1	4.7	1.08E+16	24
200710161638	-44.6978	167.2414	159/59/46	41/52/139	5.6	4.9	2.95E+16	26
200710161750	-44.7540	167.4504	13/61/69	232/36/123	4.4	3.9	8.49E+14	24
200710162323	-44.7552	167.3178	197/77/60	85/33/155	4.7	4.1	1.52E+15	20

Date (yyyymmddhhmm); S/D/R - strike/dip/rake; NP1 - nodal plane 1; NP2 - nodal plane 2;
ML - local magnitude; Mw - moment magnitude; Mo - moment (Nm); CD - centroid depth (km)

the seismic moment and mechanism are stable which indicates a well resolved solution. The main shock has a predominantly reverse faulting mechanism with a NW-SE trending compression axis which, along with a depth of 21 km, is consistent with rupture on the plate interface. All the aftershocks are also predominantly reverse faulting mechanisms with depths of 20 – 25 km; however, the largest aftershock and several other events have the strike of the east dipping fault plane rotated by around 40° counter-clockwise relative to the main shock.
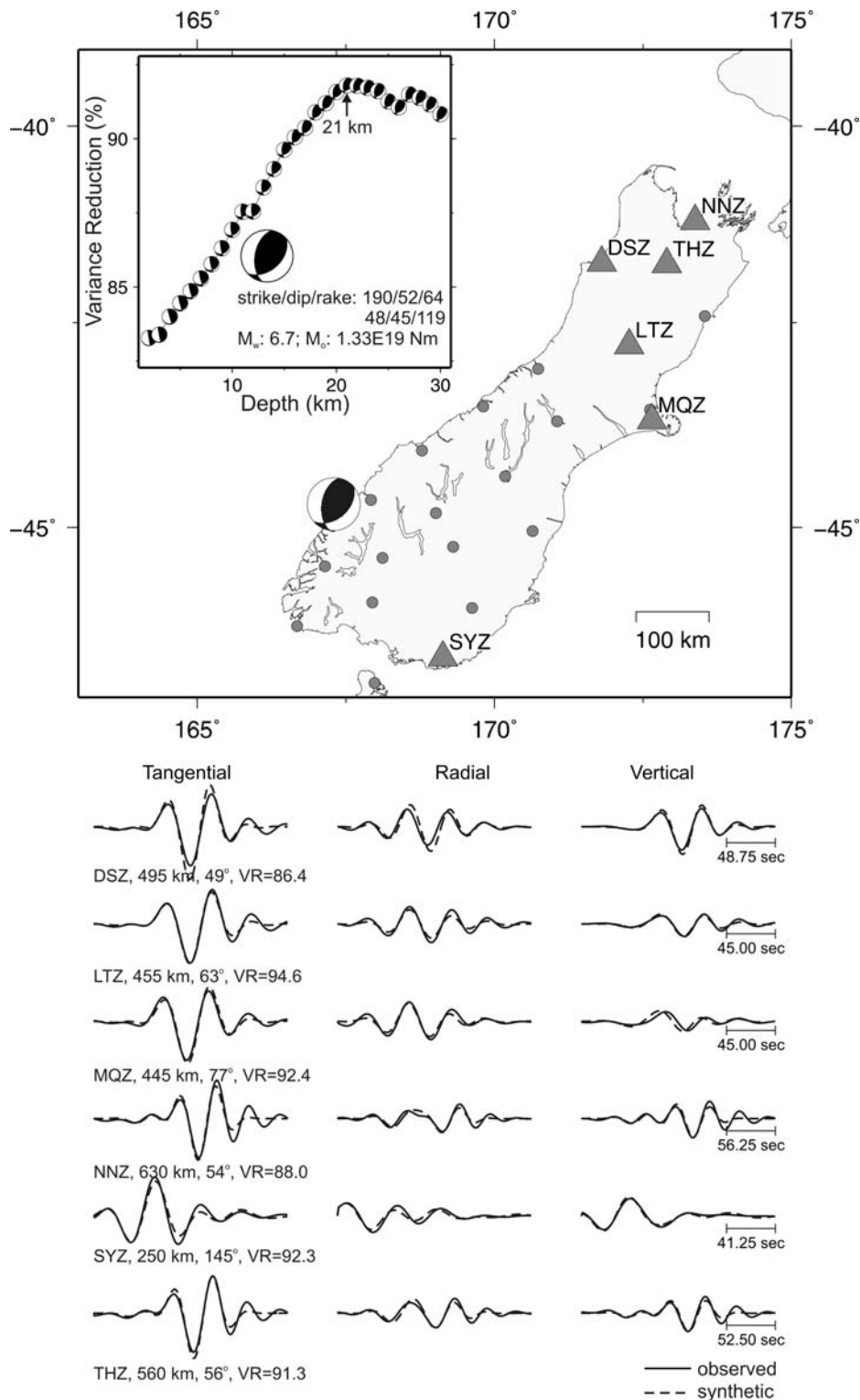
Figure 4: Location and focal mechanism of the main shock and the stations used to calculate the CMT solution. Stations that were not used in the inversion are indicated by the black dots. Most of the broadband stations in the southern half of the South Island clipped during the event and could not be used. The fits between the observed (solid) and synthetic (dashed) waveforms were excellent for all the stations used in the solution. The text beneath each waveform gives the station code, source-receiver distance, source-receiver azimuth and variance reduction for that station respectively. The variance reduction versus depth plot gives the largest variance reduction between the observed and synthetic waveforms at a depth of 21 km For depths greater than ~ 15 km the seismic moment and mechanism are stable. The seismic moment varies from 1.12×10^{19} – 1.31×10^{19} Nm over a depth range of 15 – 30 km. Also shown are the parameters for the best fit solution at 21 km.
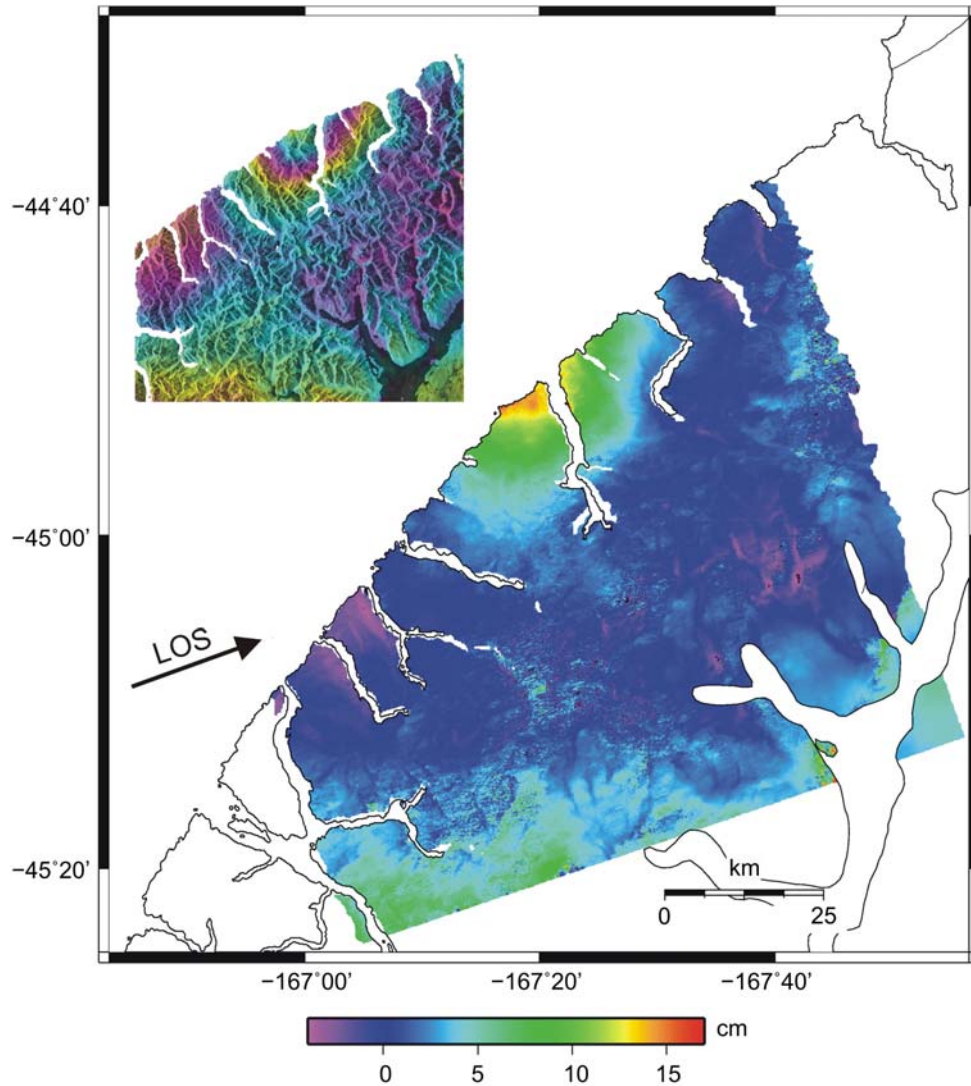
Figure 5: Wrapped differential interferogram (top) and geocoded unwrapped differential interferogram (bottom) derived from two ascending ALOS PALSAR images (path 347, frames 6270, shift -3) acquired in 2007 on 06-Sept and 07-Dec (Bp = 831 m). The arrow shows the LOS direction. Coseismic displacements of the 2007 George Sound earthquake are observed in the centre of the image with maximum LOS value of approximately 15 cm.

Figure 6: Wrapped differential interferogram calculated from ALOS PALSAR images acquired on 22-Oct and 22-Jan. A post seismic signal is observed around the coast west of George Sound with a maximum LOS   value around 5 cm.

GEODETIC DATA AND MODELLING

Satellite radar data

The DInSAR technique works by comparing the travel times of radar waves backscattered from the ground to the satellite, between two images taken at different times. Once the contributions due to satellite orbits and ground topography were removed, and provided the two images are coherent, the ground deformation that occurred between the times the two images were obtained can be displayed as an interference pattern or interferogram. For the PALSAR instrument, which emits L-band radar (24 cm wavelength), one fringe of phase

difference (seen on Figure 5 as a change in colour from blue, through green and red, and back to blue) represents about 12 cm of ground motion in the direction along the line-of-sight (LOS) from the ground pixel to the satellite. Phase shifts are resolvable only relative to other points in the interferogram, but absolute deformation can be inferred by assuming one area in the interferogram (for example, a region away from expected deformation sources) experienced no deformation, or by using ground control (GPS or similar) to establish the absolute movement of a point. It is often possible to decompose LOS deformation into three components by introducing assumptions on the nature of deformation or by using ground control data [e.g., 16].

In this work, four PALSAR images acquired in 2007/2008 (06-Sept, 22-Oct, 07-Dec-2007 and 22-Jan-2008) were used to calculate two coseismic (06-Sept and 22-Oct, 06-Sept and 07-Dec) and two postseismic (22-Oct and 07-Dec, 22-Oct and 22-Jan) differential interferograms using GAMMA software. The topographic component was removed using the Land Information New Zealand (LINZ) 40-metre resolution digital elevation model (DEM). The interferograms were filtered with adaptive filter [17] and unwrapped. The GAMMA software was used to reduce topographic effects and orbital inaccuracies. The resulting wrapped and unwrapped interferograms derived from two ALOS PALSAR images acquired on 06-Sept and 07-Dec are presented in Figure 5. This image includes the coseismic signal and any postseismic signal in the 6 weeks following the earthquake.
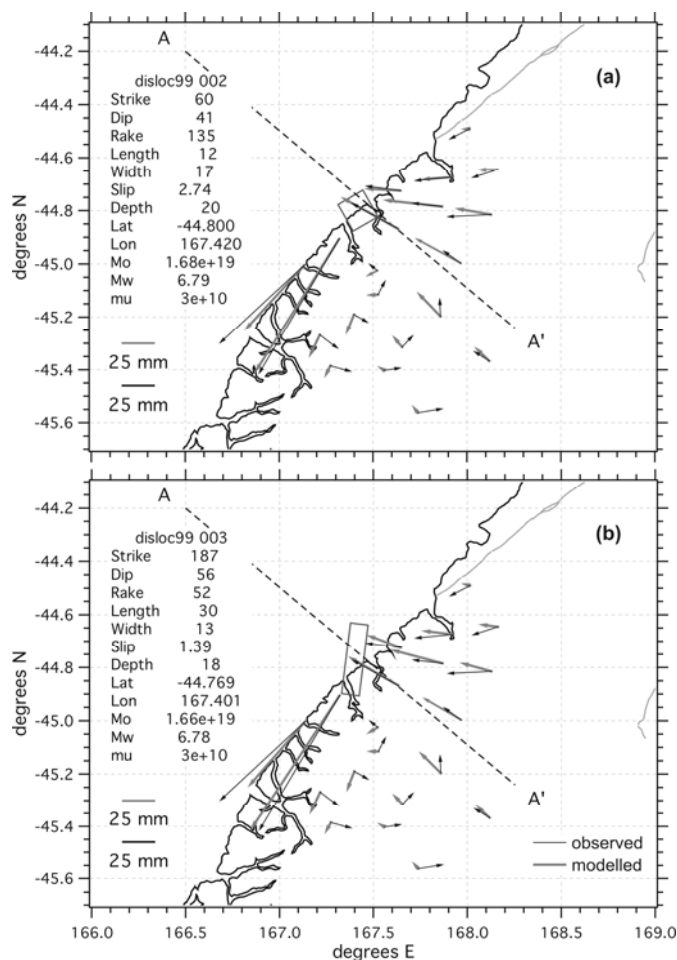
Coseismic displacements are well observed around the coastline in the centre of the image; this is true of all interferograms whose time span includes the earthquake. An apparent postseismic signal is also observed on the 22-Oct to 22-Jan interferogram (Figure 6). Atmospheric disturbances and residual topographic signals are also present throughout the images. The cause of a large region of negative displacement around the coastline southwest from the main shock is unknown; however, its value increases with time until the date of the last available observation (22-Jan-2008) so it does not appear to be directly linked to the 2007 earthquake.
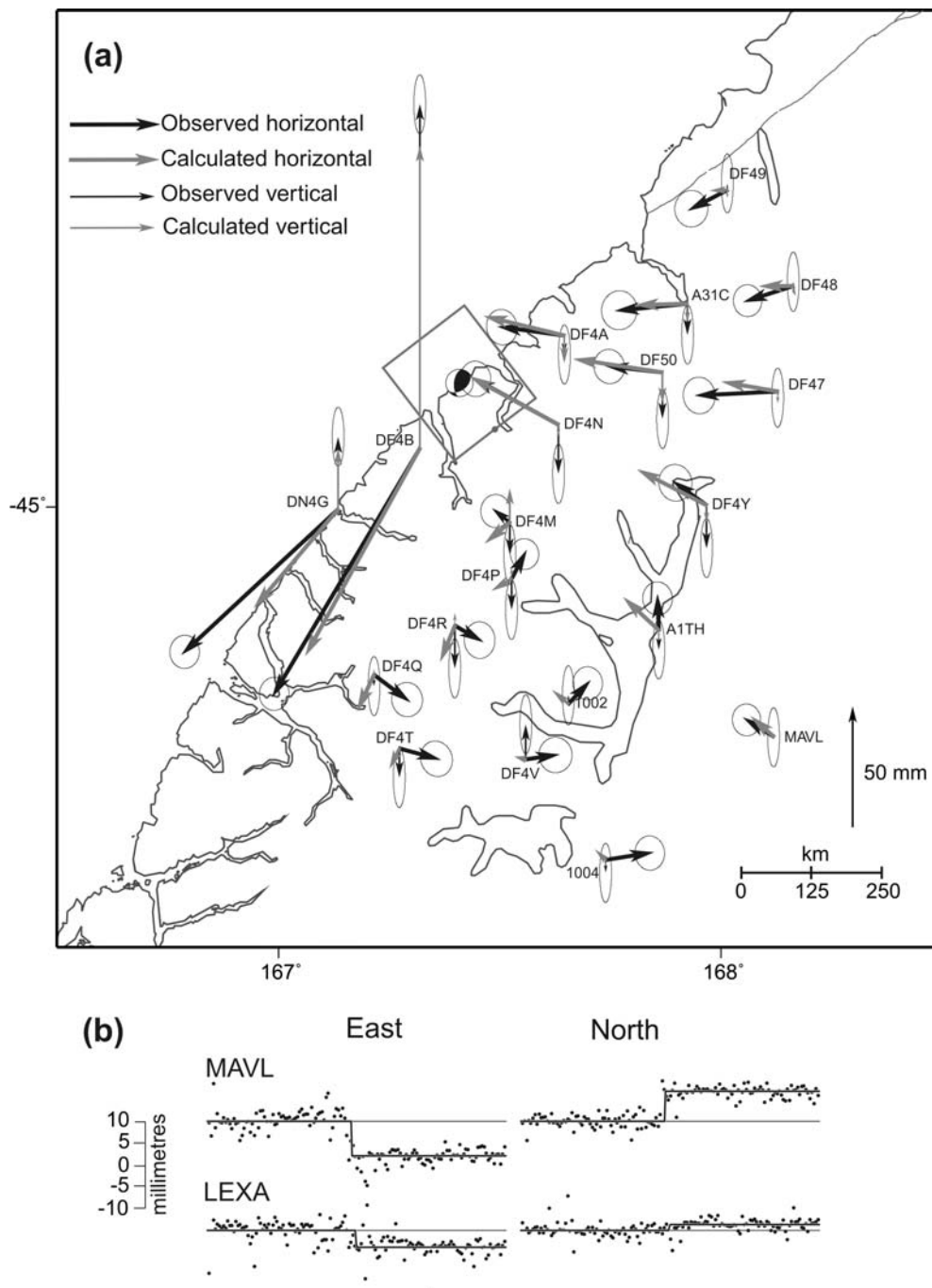
GPS data

Survey-mode GPS (sGPS) data were collected about 4 weeks after the main shock from 19 sites in the vicinity of the earthquake (Figures 7, 8). Pre-earthquake data were collected at all these sites in February 2001 and February 2006, and there were a number of observations at other times for several of the sites, especially those in the vicinity of the 2003 Secretary Island earthquake. Each occupation of a site, which usually lasts from 2-3 days, provides a site position with an accuracy of a few millimetres. We estimated the interseismic velocities at these sites using an updated version of the deformation model of [18], avoiding data intervals that included coseismic offsets. By differencing the November 2007 and February 2006 position estimates and applying the interseismic correction, we obtain an estimate of the coseismic displacement at these 19 near-field sites as well as at other far-field sites.

We did not use all available cGPS data in our analysis, but since only two cGPS sites recorded displacements above the

Figure 7: Maps of observed coseismic displacement (black arrows) at sGPS stations, after correction for (assumed steady) interseismic displacement. Also shown are the modelled displacements (grey arrows) when the sGPS data alone are inverted to define the fault parameters. Only horizontal displacements are shown, but both vertical and horizontal observations were used in the inversion. The grey rectangle shows the surface projection of the fault plane, and other parameters are given in Table 2. (a) Shows the solution when an east-dipping fault plane is assumed and (b) Shows the solution for a west-dipping fault plane.

Figure 8: (a) Map of fits to sGPS data when sGPS and DInSAR data are inverted simultaneously. Arrow thickness correspond to horizontal and vertical observed and calculated vectors as shown. Error ellipses on observed vectors are at 95% confidence. Grey box shows the modelled uniform-slip fault plane, and the beachball represents the slip mechanism. (b) Detrended time series of continuous GPS sites MAVL and LEXA (see Figure 1 for location). The solid line shows the expected displacements for the model used in (a).

noise level we do not think this is a significant problem. We did use data from three of the cGPS sites, LEXA, MTJO and OUSD, but these were treated as sGPS stations. In other words, we only used their data from days on which other sGPS stations were deployed.

Inversions of geodetic data

We inverted the geodetic data using sGPS alone, and using a combination of the sGPS and DInSAR data. In the first case we inverted the coseismic displacements and used a non-linear least squares method (disloc99 software; [19]) to estimate the parameters of the earthquake source (latitude, longitude, depth, strike, dip and rake of the double-couple mechanism,

along-strike length and down-dip width of a planar fault, and uniform slip magnitude on that plane) assuming an elastic half-space model. We used the full covariance matrix, taken from the GPS processing, for the horizontal displacement data, and treated the vertical data as independent parameters, each with the uncertainty estimated during the GPS processing. The formal uncertainties from the GPS processing were scaled by a factor of 5 (covariance matrix scaled by 25) to take account of unmodelled correlations in the GPS data; this scaling value is based on many years' experience. The results are shown in Table 2 and Figure 7.

In the second method we modelled the sGPS and DInSAR data in a joint inversion, using a modified version of DEFNODE software [20; 21] and solving for the same

Table 2: Estimated source parameters, east-dipping fault plane[*]

Parameter	Geodetic, sGPS only	sGPS, cGPS, DInSAR	Moment tensor	Strong motion
Strike	60 ± 6°	52 ± 2°	48°	54° (fixed)
Dip	41 ± 5°	43 ± 2°	45°	44° (fixed)
Rake	135 ± 6°	127 ± 2°	119°	129°
Depth	20 ± 2 km	18.1 ± 0.5 km	21 km	17-21 km (inverted)
Slip amount	2.7 ± 1.5 m	0.94 ± 0.09 m	-	1.02 m[**]
Length	12 km (fixed)[****]	18 ± 2 km	-	12 km[***']
Width	17 ± 2 km	29 ± 2 km	-	25 km[***"]
Latitude	44.80 ± 0.01°S	44.80 ± 0.01°S	44.721 °S (fixed)	-44.8° (fixed)
Longitude	167.42 ± 0.01°E	167.41 ± 0.01°E	167.302°E (fixed)	167.4° (fixed)
Moment[*****]	1.7×10^{19} Nm	1.5×10^{19} Nm	1.3×10^{19} Nm	0.98×10^{19} Nm
M_w	6.78	6.75	6.72	-
χ_n^2 [******]	7.7	2.51	-	-

[*] We assume uniform slip on a planar rectangular fault buried in an elastic half space.

[**] Average slip over the elliptical surface

[***'] Ellipse minor axe

[***"] Ellipse major axe

[****] disloc99 was unable to solve for all 9 parameters, so we fixed the length at a value that gave a stable solution with the lowest χ_n^2.

[*****] Using rigidity $\mu = 3 \times 10^{10}$ Nm^{-2} for geodetic modelling.

[******] χ_n^2 is much lower in the combined inversion because of the relatively good fit to the large number of DInSAR data. The goodness-of-fit may be misleading because we have ignored correlations between nearby data points in the smoothed DInSAR image.

parameters, plus the offset in the DInSAR as an additional parameter. We used the same sGPS displacements and uncertainties as in the first method. We used the 06-Sep to 22-Oct DInSAR image and resampled every kilometre for a total of 391 observations.

We assumed these displacement estimates were independent, and assigned each one an uncertainty of 10 mm based on a comparison between DInSAR and sGPS displacements resolved to line-of-sight at the sGPS stations. The full covariance matrix of the GPS displacements was not used in this inversion; we assumed independent data and used the uncertainty assigned to each observation plus the east-north correlation at each station. Formal uncertainties in the parameters were estimated by assuming a linear set of equations and a Gaussian noise distribution.

Survey-mode GPS sites to the north and east of the quake were fit fairly well while those to the south were poorer (Figures 7, 8). The two largest displacements, at sites southwest of the quake, were fit much better in the sGPS-only inversion than in the combined inversion. The fit to the DInSAR image in the combined inversion was excellent (Figure 9). Forward modelling of the sGPS-only solution gave a poor fit to the DInSAR image. The overall fit to the sGPS data is less good by about a factor of 3 than we would normally expect. Possible reasons for this are that the interseismic correction was not sufficiently accurate, that some near-source sites experienced local displacement due to strong shaking, or that our simple uniform-slip models are not detailed enough.
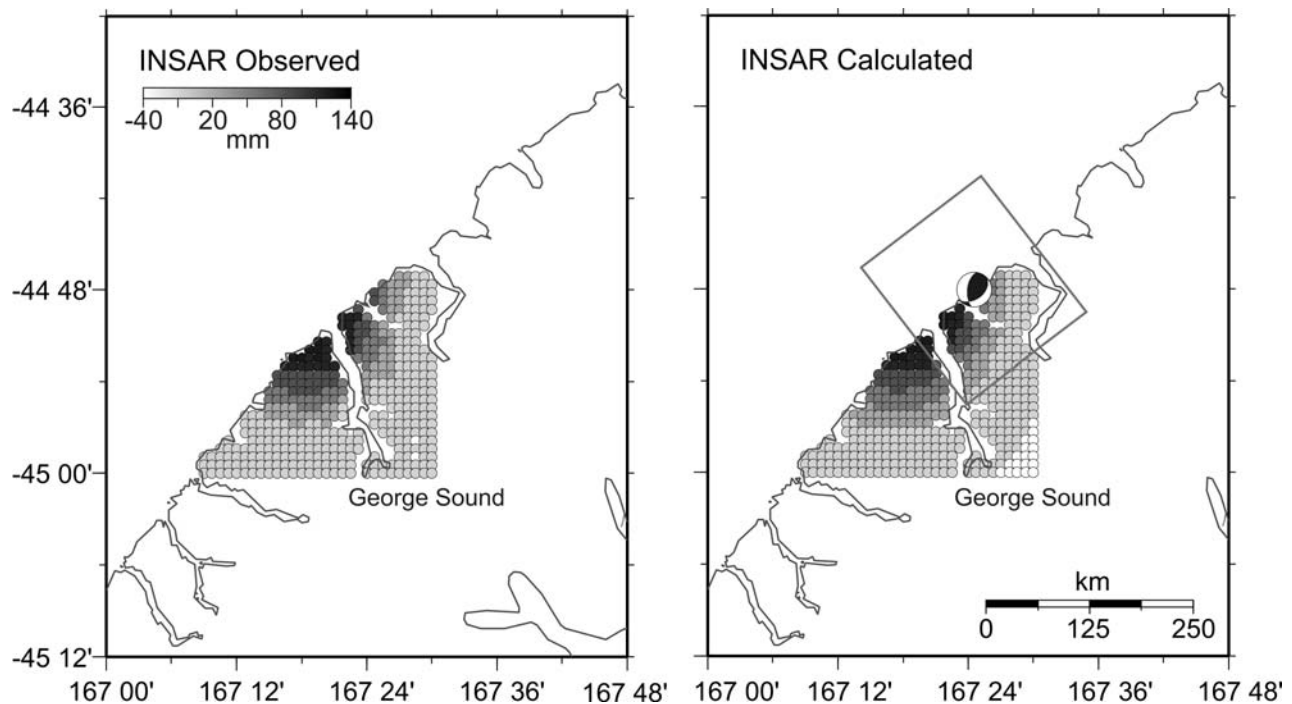
Figure 9: Maps of observed and calculated DInSAR line-of-sight displacements in millimetres. Grey box shows the modelled uniform-slip fault plane, and the beachball represents the slip mechanism.
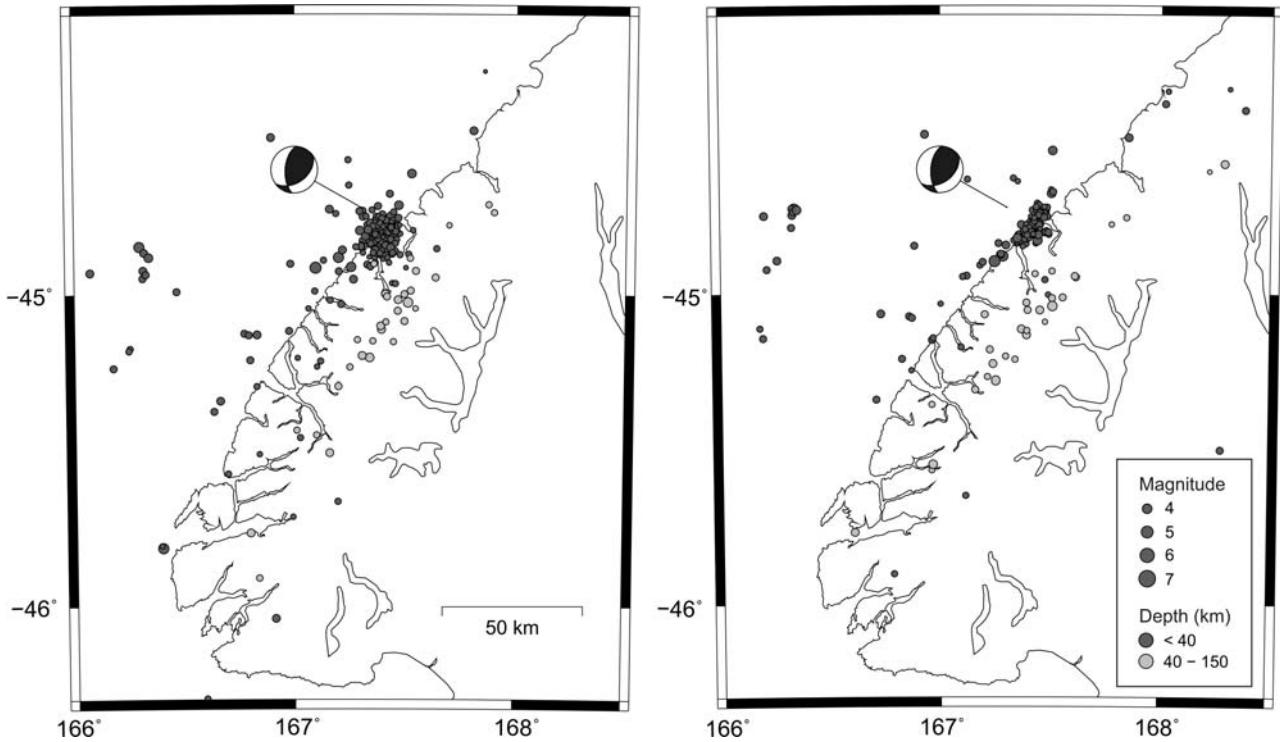
Figure 10: Locations for 220 aftershocks, recorded between 17 October and 27 November 2007, before (left panel) and after (right panel) adding the five portable stations to the data set. The GeoNet aftershock deployment significantly improved the location accuracy.

Even though there is some inconsistency between the two data sets, the solutions for the earthquake fault parameters (Table 2) are quite similar, and are also similar to those derived by seismological methods. The main difference is a trade-off between fault area and slip magnitude in the two cases. The small areal extent of the aftershock distribution (Figure 10) and the concentration of slip in the strong-motion inversion (Figure 12) both suggest a smaller area and higher slip magnitude.

The solution that best fits the 2007 George Sound earthquake is of an east-dipping thrust plane extending beneath the coast. The geodetic moment is similar to the seismological estimate (1.5×10^{19} and 1.3×10^{19} Nm, respectively), suggesting that no major after-slip occurred. The closest cGPS site, MAVL, also shows no indication of afterslip in its time series, despite the possible postseismic deformation observed in the 22-Oct/22-Jan DInSAR image.

A model in which the complementary (west-dipping) plane ruptured was also tried. Using the sGPS-only data set we could obtain an equally good fit to the data (Figure 7), though the correspondence between the fault plane and aftershocks was less favourable than in the east-dipping case. Using the combined data, the normalized goodness-of-fit statistic, χ_n^2, of the west-dipping solution was somewhat worse than the east-dipping one, with the source moving well offshore and covering an area much larger than the aftershock zone. Also, the residuals to the DInSAR image were significantly non zero in the west-dipping case. We therefore favour the east-dipping solution.

AFTERSHOCK LOCATIONS

The large station spacing of the permanent GeoNet seismic network makes it difficult to locate the smaller aftershock earthquakes accurately. In order to improve hypocenter locations the data acquired by the five portable short-period seismometers were incorporated into the GeoNet network data by running a triggering algorithm [22]. The P- and S-picks were then manually refined. The portable stations, located relatively close to the epicentre (~15-30 km; Figure 2),

provided high quality aftershock data for about 40 days. The newly acquired data set was processed using standard New Zealand earthquake location methods with a 1-D velocity model. The velocity model has a very simple 3-layer velocity structure and is not specific for the Fiordland region.

A total number of 220 earthquakes were located in or near the aftershock zone, with magnitudes (M_L) ranging from 2.0 to 4.7. The new hypocenter solutions are greatly improved from the ones calculated using solely the permanent GeoNet network (e.g. the average standard error, S.E., decreased from about 0.4 to 0.09 seconds). Figure 10 shows the improved epicentre locations. The main shock is expected to be located within the aftershock zone, but in the preliminary determination of hypocenters presented here it is farther west from shore than the aftershocks, presumably because the complex Fiordland velocity structure was not taken into account. Although the same velocity models were used for main shock and aftershock locations, the main shock location had a much smaller number of seismometer stations available close by, causing it to be less accurate. This problem will be addressed in future studies by using double-difference relocation methods and a 3D-velocity model specific for the Fiordland region, but for now we can assume that the main shock is likely co-located with the deeper group of aftershocks.

The aftershock locations viewed in cross-section reveal two very distinct earthquake clusters (Figure 11). The larger aftershocks define a steeply SE-dipping plane between about 17 and 25 km depth. We suggest that this cluster represents the plate interface. Another cluster at about 7-12 km depth is composed of smaller earthquakes on a NW-dipping plane within the overlying plate. A number of deeper (> 25 km) earthquakes image the continuation of the subducted slab down to about 130 km depth. The suggested location of the plate interface (Figure 11) is consistent with the centroid depth (21 km) and fault plane dip (45°) from the moment tensor solution for the main shock. Earthquake relocation methods using a detailed 3D-velocity model may change the dip of the 17-25 km deep aftershock cluster towards the calculated fault plane dip of 45°.
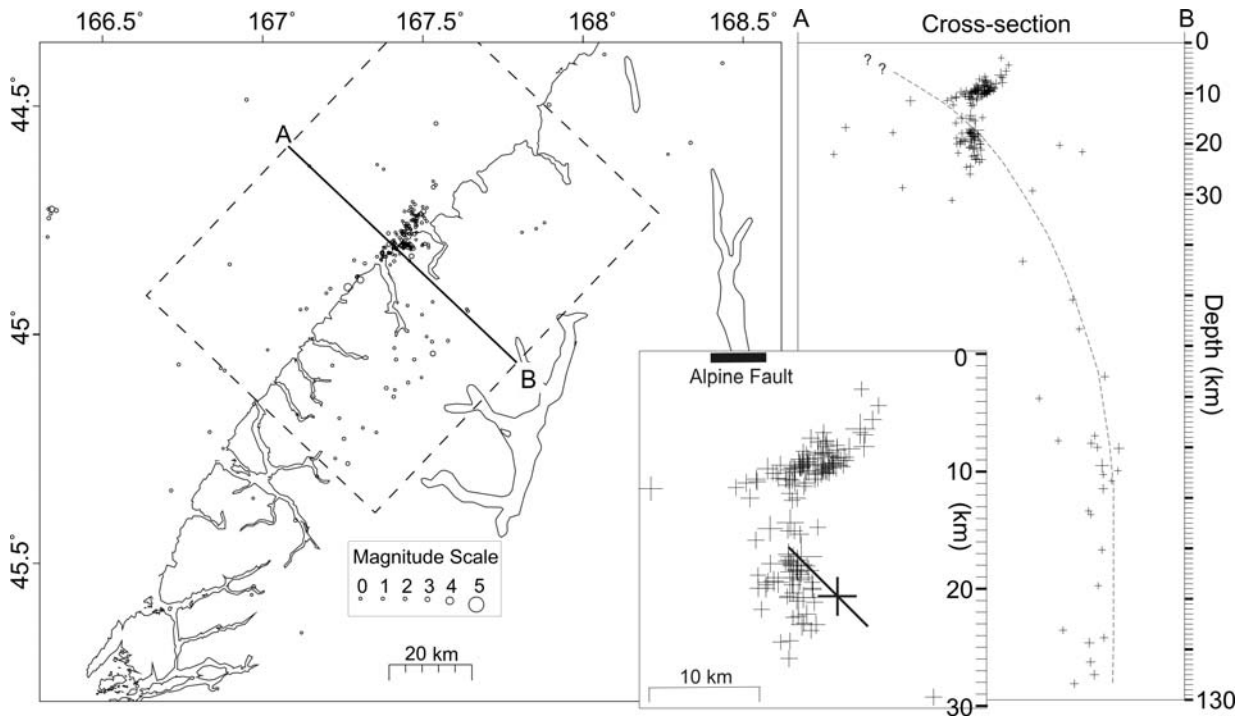
Figure 11: *Aftershock locations viewed in cross-section. Two distinct earthquake clusters are visible. The estimated plate interface is indicated by the dashed line. The main shock is expected to be located within the aftershock zone. The black cross and thick solid line within the cross-section indicate the centroid depth of 21 km and fault plane dip of 45º given by the CMT solutions; the black bar marks the approximate location of the Alpine Fault according to [23].*

STRONG MOTION INVERSION

To solve for a detailed slip and the rupture time distribution, we inverted data from the 8 closest strong motion sites of the GeoNet network (Figure 12). Seismograms were band pass filtered between 0.01 and 0.1 Hz and integrated once to obtain velocity data. We inverted for 3 elliptical rupture source areas distributed with variable position and angle within the fault plane and with variable rupture velocity, slip and rake [24; 25].

We tested two fault planes, following the solution from the CMT inversion. However, the best waveform fits were
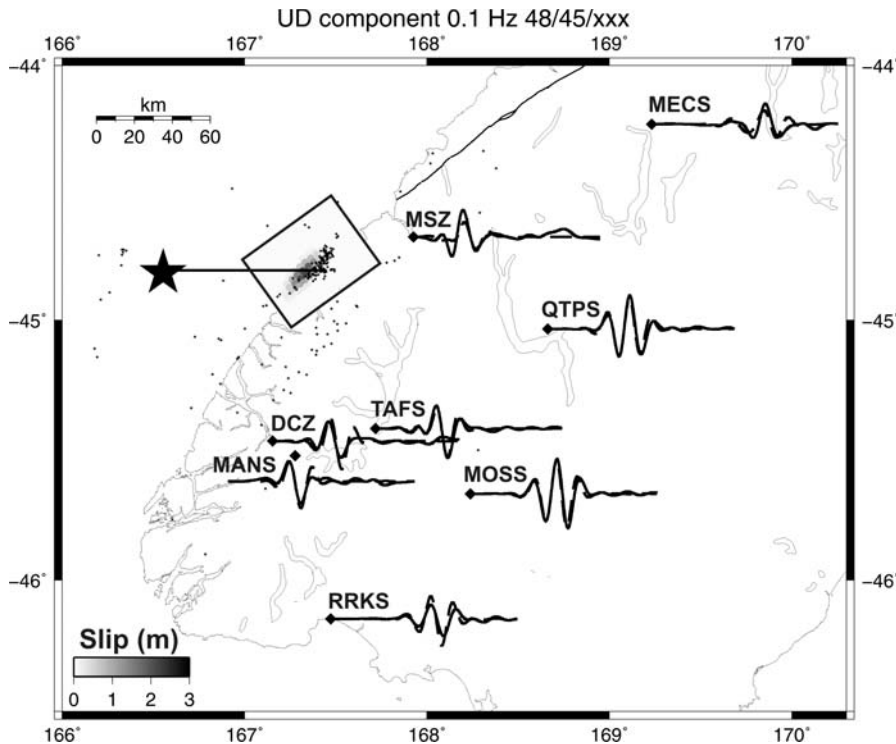

Figure 12: *Slip distribution (m) projected onto the surface and the waveform fit between observed (solid) and synthetic (dashed) data filtered up to 0.1 Hz. Stars indicate the aftershocks. The large black star represents a location of 44.8°S, 167.4°E and depth 20 km, close to the centroid of the geodetic fault plane solutions.*

obtained for the east dipping fault plane (strike 48°, dip 45°). The possible fault plane area in the model is 48 by 48 km², divided into 256 3x3 km² subfaults. The fault plane location (yellow star on Figures 12 and 13) is placed closer to shore than the initial GeoNet location, in order to match the area defined by the refined aftershock relocations. However, the rupture is free to start anywhere on the plane.

Our best slip distribution (Figure 13) is dominated by one elliptical slip patch of 25 km and 17 km principal axis lengths and maximum slip 2.1 m. It is located at depths between 17 and 21 km. We also obtained a rake angle value for this patch of 122°, similar to the one obtained from moment tensor inversion. The rupture starts with very little slip that can not be resolved properly with 0.1 Hz filtered data since it gets mixed up with the main patch. Then the rupture front breaks the main patch after 7 seconds, reaches a maximum slip of 2.1 m after 9 seconds, and terminates after 12 seconds. The moment value calculated for this solution is 9.13×10^{18} Nm. We also computed an estimated overall stress drop value of 6 MPa.

This kinematic solution is consistent with the solution from the GPS, InSAR and teleseismic inversions with a similar fault plane orientation and source dimensions. Further studies will involve inverting for data filtered at high frequencies in order to retrieve more details of the fault rupture mechanism.
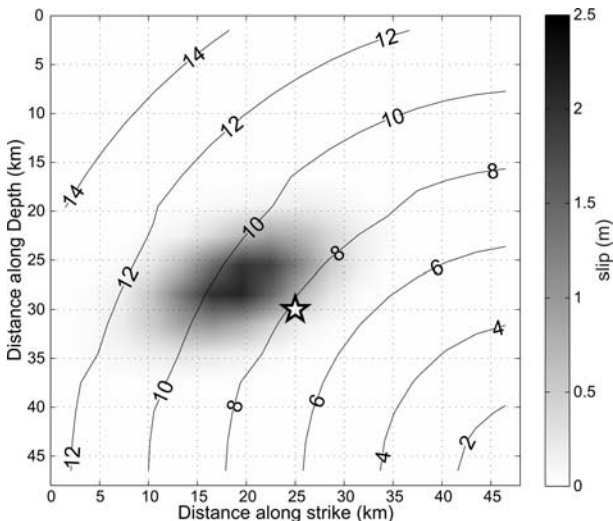
Figure 13: *Final slip distribution (m) on a 48 by 48 km² fault plane, dipping eastward, using velocity data filtered from 0.01 to 0.1 Hz. The slip distribution is characterized by one single patch of maximum slip 2.1 m (after 9 seconds) and dimensions about 25 by 17 km². The star represents a location of 44.8°S, 167.4°E and depth 20 km, close to the centroid of the geodetic fault plane solutions. The contours represent rupture time in seconds.*

DISCUSSION

A number of different geophysical tools were used to monitor and analyse the M_w 6.7 George Sound earthquake and its aftershock sequence. The moment tensor analysis indicates that the main shock is located at a depth of 21 km and was caused by a reverse faulting mechanism with a NW-SE trending compression axis. Several independent techniques indicate that the main fault plane dips towards the east, suggesting that this thrust event is likely to be a subduction interface event. A rupture along the plate interface is also

consistent with the distribution of the larger aftershocks. The stress drop estimated by strong motion modelling is 6 MPa, within the normal range for subduction thrust events. The rupture is characterized by a very small initial pulse followed by a main pulse that reaches a maximum slip of 3.1 m after 8 seconds and terminates after 14 seconds. Coseismic surface displacements on land within the George Sound area are well recorded by satellite radar interferometry and survey-mode GPS. The InSAR and sGPS data are consistent with the main shock being a thrust event at about 20 km centroid depth. The preliminary geodetic inversions suggest an east-dipping rupture plane extending beneath the coast; after-slip up to about 10% of the coseismic slip could have occurred in the 4-6 weeks following the main shock and early aftershocks.

Preliminary results from the multi-discipline geophysical data set used to characterize the 2007 George Sound earthquake uniformly suggest a subduction interface event along an eastward dipping plane that is located at about 20 km depth just offshore of Fiordland. The earthquake was related to convergence of the Australian and Pacific plates rather than to intra-plate stresses. More detailed studies of aftershock focal mechanisms and stress distributions are needed to determine the effects that the earthquake had on the nearby Alpine Fault; i.e. to examine whether or not the Coulomb failure stress increased on this fault. Double-difference and 3D-relocation methods will provide more detailed information on location and dip of the main shock fault plane and aftershocks.

REFERENCES

1 Reyners, M., Gledhill, K. & Waters, D. (1991). "Tearing of the Subducted Australian Plate during the Te Anau, New Zealand, Earthquake of 1988 June 3". *Geophysical Journal International* **104** (1): 105-115.

2 Robinson, R., Webb, T., McGinty, P., Cousins, J. & Eberhart-Phillips, D. (2003) "The 2000 Thompson Sound Earthquake, New Zealand". *New Zealand Journal of Geology & Geophysics* **46**: 331–341.

3 Reyners, M. & Webb, T. (2002) "Large earthquake near Doubtful Sound, New Zealand 1989-93". *New Zealand Journal of Geology and Geophysics* **45**: 109-120.

4 McGinty, P. & Robinson, R. (2007) "The 2003 M_w 7.2 Fiordland subduction earthquake, New Zealand:

aftershock distribution, main shock fault plane and static stress changes on the overlying Alpine Fault". *Geophysical Journal International* **169**: 579–592.

5 Reyners, M., McGinty, P., Cox, S., Turnbull, I., O'Neill, T., Gledhill, K., Hancox, G., Beavan, J., Matheson, D., McVerry, G., Cousins, J., Zhao, J., Cowan, H., Caldwell, G., Bennie, S. & the GeoNet team (2003) "The M$_W$7.2 Fiordland earthquake of August 21, 2003: Background and preliminary results". *Bulletin of the New Zealand Society of Earthquake Engineering* **36**(4): 233-248.

6 Beavan, J., Tregoning, P., Bevis, M., Kato, T. & Meertens, C. (2002) "Motion and rigidity of the Pacific plate and implications for plate boundary deformation". *Journal of Geophysical Research* **107** (B10), 2261, doi:10.1029/2001JB000282.

7 DeMets, C., Gordon, R., Argus, D. & Stein, S. (1994) "Effect of recent revisions to the geomagnetic reversal time scale on estimates of current plate motions". *Geophysical Research Letters* **21**: 2191-2194.

8 Eberhart-Phillips & Reyners (2001) "A complex, young subduction zone imaged by three-dimensional seismic velocity, Fiordland, New Zealand". *Geophysical Journal International* **146**: 731–746.

9 Reyners, M., Robinson, R., Pancha, A. & McGinty, M. (2002) "Stresses and strains in a twisted subduction zone - Fiordland, New Zealand". *Geophysical Journal International* **148**: 637-648.

10 Massonnet, D. & Feigl, K. (1998) "Radar interferometry and its application to changes in the Earth surface". *Reviews of Geophysics* **36**(4): 441-500.

11 Rosen, P.A., Hensley, S., Joughin, I.R., Li, F.K., Madsen, S.N., Rodriguez, E. & Goldstein, R.M. (2000) "Synthetic aperture radar interferometry". *Proceedings of the IEEE* **88** (3): 333-382.

12 Ristau, J. (2008) "Implementation of routine regional moment tensor analysis in New Zealand". *Seismological Research Letters* **79**: 400-415.

13 Dreger, D. & Helmberger, D.V. (1993) "Determination of source parameters at regional distances with single station or sparse network data". *Journal of Geophysical Research* **98**: 8107-8125.

14 Pasyanos, M.E., Dreger, D.S. & Romanowicz, B. (1996) "Towards real-time determination of regional moment tensors". *Bulletin of the Seismological Society of America* **86**: 1255-1269.

15 Dreger, D.S. (2003) "TDMT_INV: Time Domain Seismic Moment Tensor INVersion". Internation Handbook of *Earthquake and Engineering Seismology* **81** B: 1627.

16 Samsonov, S., Tiampo, K., Rundle, J. & Li, Z. (2007) "Application of DInSAR-GPS optimization for derivation of fine scale surface motion maps of southern California". *Transactions on Geoscience and Remote Sensing* **45** (2): 512-521.

17 Goldstein, R.M. & Werner, C.L. (1998) "Radar Interferogram Filtering for Geophysical Applications". *Geophysical Research Letters* **25** (21): 4035-4038.

18 Beavan, J. & Haines, J. (2001) "Contemporary horizontal velocity and strain-rate fields of the Pacific-Australian plate boundary zone through New Zealand". *Journal of Geophysical Research* **106** (B1): 741–770.

19 Darby, D. J. & Beavan, J. (2001) "Evidence from GPS measurements for contemporary plate coupling on the southern Hikurangi subduction thrust and partitioning of strain in the upper plate". *Journal of Geophysical Research* **106** (B12): 30,881-30,891.

20 McCaffrey, R. (1995) "DEFNODE users guide". Rensselaer Polytechnic Institute, Troy, New York, www.rpi.edu/~mccafr/defnode.

21 McCaffrey, R. (2002) "Crustal block rotations and plate coupling, in Plate Boundary Zones". Eds. S. Stein and J. Freymueller, *AGU Geodynamics Series* **30**: 100-122.

22 Gledhill, K. (1985) "An earthquake detector employing frequency domain techniques". *Bulletin of the Seismological Society of America* **75** (6): 1827-1835.

23 Barnes, P.M., Sutherland, R., Delteil, J. (2005) "Strike-slip structure and sedimentary basins of the southern Alpine Fault, Fiordland, New Zealand". *Geological Society of America* **117** (3/4): 411-435.

24 Francois-Holden, C., Di Carli, S., Sladen A. & Madariaga R. (2008) "Non linear kinematic source inversion of the 2000 Tottori, Japan earthquake". - submitted *Geophysical Research Letters*.

25 Peyrat, S. & Favreau, P. "Kinematic and spontaneous rupture models of the 2005 Tarapaca intermediate depth earthquake" -submitted *Geophysical Journal International.*

26 Wessel, P. & Smith, W.H.F. (1998) "New, improved version of the Generic Mapping Tools". *EOS Transactions of the American Geophysical* **79**: 579.2